

Effect of Welding Thermal Cycling on Microstructures and Cryogenic Impact Toughness of Medium-Mn Low-Temperature Steel



QING SUN, YU DU, XIAONAN WANG, TAO LIU, ZHEN TAO, LEI LI, ZHIHUI LIAO, and LINXIU DU

This work studied the effect of welding thermal cycling on the microstructures and cryogenic impact toughness of medium-Mn low-temperature steel by single-pass welding thermal simulation test. The microstructures of the heat-affected zone (HAZ) were characterized by optical microscopy, electron backscatter diffraction, X-ray diffraction, and transmission electron microscopy. The results indicated that the microstructures of fine-grain HAZ are fine-lath martensite with film-like retained austenite in the heat input range of 10 ~ 30 kJ/cm. Meanwhile, fine-grain HAZ has excellent low-temperature impact toughness, and the impact energy tested at $-40\text{ }^{\circ}\text{C}$ can reach about 245 J. The coarse martensitic packet and block in the coarse grain HAZ seriously deteriorated the cryogenic impact toughness, and the greater the heat input, the worse the cryogenic impact toughness. The impact energy tested at $-40\text{ }^{\circ}\text{C}$ was 71 J when the heat input was 10 kJ/cm. The cryogenic impact toughness of HAZ gradually deteriorated with the peak temperature increase because of the decrease of retained austenite content and the increase of martensitic lath width.

<https://doi.org/10.1007/s11661-024-07521-6>

© The Minerals, Metals & Materials Society and ASM International 2024

I. INTRODUCTION

LOW-TEMPERATURE steel is generally served in low-temperature environments at $-20\text{ }^{\circ}\text{C}$ to $-196\text{ }^{\circ}\text{C}$. It is widely used in the storage and transportation process of liquefied petroleum gas, natural gas and other energy sources. At present, nickel-based steels occupy a dominant position in the field of low-temperature steel.^[1-3] However, high nickel content inevitably leads to a sharp increase in production costs.^[4,5] In recent years, many researchers have adopted the composition design idea of “replacing Ni with Mn”, and finally obtained a series of medium-Mn low-temperature steels with excellent cryogenic impact toughness by improving the rolling and heat treatment processes.^[6-9]

Welding is one of the leading manufacturing methods for offshore structures, low-temperature pressure vessels, *etc.* Due to the influence of the welding thermal

cycle, the mechanical properties of the welded joint have changed compared to the base material. The microstructure of steel with excellent strength and toughness is damaged by the rapid heating and cooling during the welding process, finally forming the heat-affected zone (HAZ) with severe deterioration of strength and toughness. HAZ undergoes different welding thermal cycles at different distances from the weld seam center, resulting in significant differences in its microstructures and mechanical properties. HAZ is generally divided into intercritical HAZ (ICHAZ) with temperatures between A_{C1} and A_{C3} , fine-grained HAZ (FGHAZ) with temperatures slightly higher than A_{C3} , and coarser-grained HAZ (CGHAZ) with temperatures much higher than A_{C3} . The CGHAZ has the most severe cryogenic impact toughness deterioration and is prone to embrittlement and cracks.^[10-13]

Numerous studies have shown that heat input influences the welding quality of medium-Mn low-temperature steel. Different peak temperatures are the main reason for the differences in the microstructure and properties of different zones in HAZ. The study by Chinakhov *et al.*^[14] shows that changes in heat input alter the content and distribution of Mn, thereby affecting the welding quality of welded joints. The high volume fraction and stability of RA in HAZ have a positive effect on the toughness improvement of medium-Mn steel.^[15] However, overly stable RA is not

QING SUN, TAO LIU, ZHEN TAO, LEI LI, ZHIHUI LIAO, and LINXIU DU are with the State Key Laboratory of Rolling and Automation, Northeastern University, Shenyang 110819, P.R. China. YU DU and XIAONAN WANG are with the School of Iron and Steel, Soochow University, Suzhou 215021, P.R. China. Contact e-mail: duydu2022@suda.edu.cn

Manuscript submitted December 19, 2023; accepted July 7, 2024.

Article published online July 21, 2024

conductive to the occurrence of the TRIP effect.^[16] Qi *et al.*^[12] used the post-weld heat treatment process to obtain a certain volume fraction of RA, and reduced the degree of local hardening of HAZ.

This paper takes a medium-Mn low-temperature steel as the research object to study the effects of different heat inputs and peak temperatures (T_p) on the microstructures and mechanical properties of the HAZ. It analyzes the reasons for the changes in RA content and stability, elucidates the mechanism of cryogenic impact toughness deterioration in HAZ, and provides a reference for developing actual welding for this medium-Mn low-temperature steel.

II. EXPERIMENTAL PROCEDURE

A. Materials

The steel used for the welding thermal simulation experiment is a medium-Mn low-temperature steel plate with a thickness of 12 mm, and the chemical composition is listed in Table I. After the thermo mechanical control process and two-step inter-critical annealing, a composite layered structure of ultra-fine-grained ferrite with RA and a small amount of martensite was obtained, achieving a good match between strength and toughness.^[6] The impact energies of experimental steel at 20 °C and - 120 °C were 308 J and 296 J. The microstructure of the experimental steel is shown in Figure 1.

B. Phase Transformation Experiment Under Welding Thermal Cycling

Sample along the rolling direction of the experimental steel and process it into Φ 4 mm \times 10 mm standard phase change instrument round rod specimen. Heat the sample at a rate of 100 °C/s to 1300 °C for 1 s on the Formast-FII phase change instrument, then cool it at a rate of 20 °C/s to 950 °C, and finally cool it to room temperature at a cooling rate of 0.1, 0.3, 0.5, 2, 5, 10, 20, 30, and 50 °C/s. The sample size and thermal expansion experimental process are shown in Figure 2.

The data collected from the experiment are analyzed by Origin to draw the thermal expansion curve and SH-CCT curve. We cut the metallographic sample at the welding thermocouple position in the middle of the sample, ground and mechanically polished it, and corroded it with a 4 pct volume fraction nitric acid alcohol solution. Subsequently, we used an Olympus optical microscope (OM) to observe its metallographic

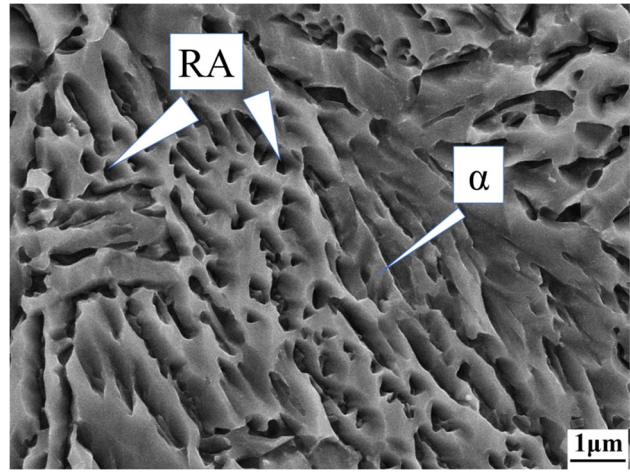


Fig. 1—The microstructure of the medium-Mn low-temperature steel.

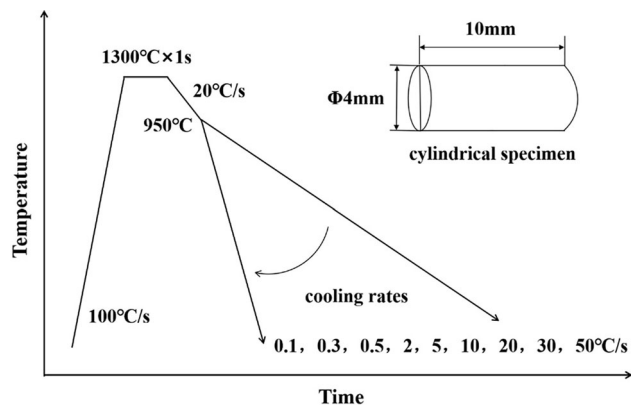


Fig. 2—Schematic diagram of thermal expansion experiment process.

structure. Finally, we used the FM-700 microhardness tester to measure the microhardness of each sample by applying a 500 g load for 10 seconds.

C. Welding Thermal Simulation Experiment

The welding thermal simulation samples were cut along the rolling direction of the experimental steel, with a size of 11 mm \times 11 mm \times 55 mm. Before the experiment starts, the samples were cleaned and wiped to remove surface oil and impurities. Each welding thermal cycle plan requires the preparation of 4 specimens, including 1 for microstructure observation and microhardness testing, and 3 for Charpy impact testing. The welding thermal simulation experiments were carried out used MS-200 thermal simulation testing machine, and Eq. [1] is the Rykalin2-D heat transfer model for simulating welding thermal cycles.^[17] Where $t_{8/5}$ is the time (s) for cooling from 800 °C to 500 °C; E is the heat input($J\ cm^{-1}$); D is the plate thickness (mm); C is the specific heat capacity($J\ g^{-1}\ ^\circ C^{-1}$); L is the thermal conductivity($W\ cm^{-1}\ ^\circ C^{-1}$); ρ is the material density($g\ cm^{-3}$); T_0 is 20 °C.

Table I. Chemical Composition of Experimental Steel (Wt Pct)

C	Ni	Mn	Si	Al	Ti	Nb	N	Fe
0.035	1.52	5.02	0.12	0.21	0.011	0.016	0.0066	bal.

$$t_{8/5} = \frac{\left(\frac{E}{d}\right)^2 \left[\frac{1}{(500-T_0)^2} - \frac{1}{(800-T_0)^2} \right]}{4\pi c l \rho} \quad [1]$$

The thermal simulation sample after the welding thermal simulation experiment was processed into a standard V-notch impact sample of 10 mm × 10 mm × 55 mm, and a V-notch was opened at the welding point of the thermocouple. The low temperature impact experiment was carried out on ZBC2452-B pendulum impact test machine, the test temperature was −40 °C, and the full heat preservation was 20 minutes. Finally, the impact fracture morphology was observed by FEIQuanta600 field emission scanning electron microscope (FE-SEM). The metallographic sample was cut, grounded, and polished, and then corroded with a 4 pct nitrate solution by volume. The microstructure was then observed under an Olympus microscope. The microhardness was measured using an FM-700 microhardness tester, applying a load of 500 g with a loading time of 10 seconds. The microstructure was characterized by FEI Tecnai G2 F20 transmission electron microscopy (SEM). Electropolishing of welding thermal simulation samples was carried out with 8 pct perchloric acid solution. The polishing parameters are voltage 19 V, current 0.7 A and time 22 s. Subsequently, electron backscattering diffraction (EBSD) was used to analyze the crystal orientation and grain boundary distribution of the microstructure. Measurement of RA volume fraction of thermal simulated specimens after welding thermal cycling using the D/max 2400 X-ray Diffractometer (XRD), calculate the volume fraction of RA using Eq. [2]^[18]:

$$V_\gamma = \frac{1.4I_\gamma}{I_\alpha + 1.4I_\gamma} \# \quad [2]$$

In the equation, V_γ is the volume fraction of RA, pct; I_γ represents $(200)_\gamma$, $(220)_\gamma$ and $(311)_\gamma$ average integral intensity; I_α represents $(200)_\alpha$ and $(211)_\alpha$ average integral intensity.

III. RESULTS AND DISCUSSION

A. Phase Transformation Behavior Under Welding Thermal Cycling

The expansion curve of experimental steel under welding thermal cycle is shown in Figure 3. Using the tangent method, the starting temperature for austenitizing of the experimental steel is 655 °C, and the ending temperature for austenitizing is 871 °C. The starting temperature of austenitization of experimental steel under welding thermal cycling conditions increased from 586 °C (equilibrium state) to 655 °C,^[6] and the ending temperature increased from 784 °C (equilibrium state) to 871 °C.

The following explanation can be given for this phenomenon: the nucleation of austenite needs to be achieved through the diffusion of carbon atoms, and the

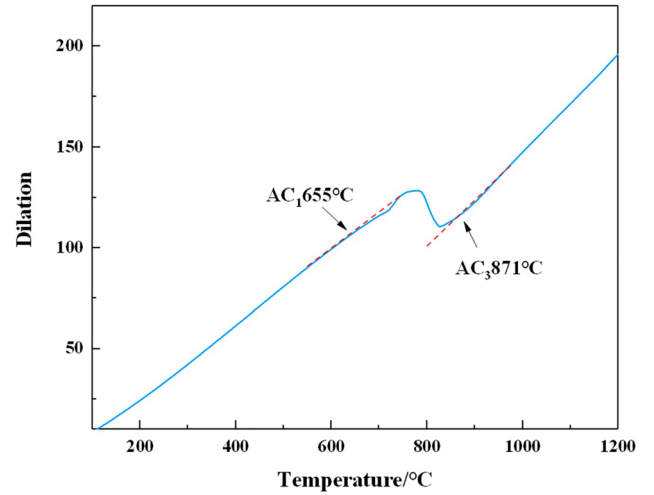


Fig. 3—Thermal expansion curve of experimental steel.

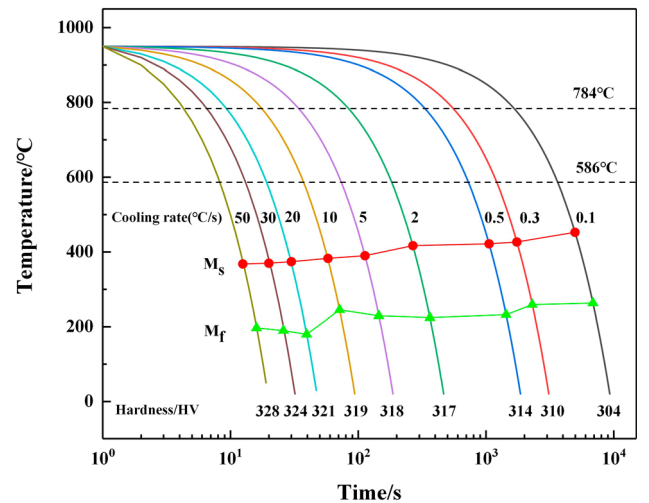


Fig. 4—Experimental steel SH-CCT curve.

time required for diffusion is called the incubation period. During the rapid heating process of the welding thermal cycle of 100 °C/s, carbon atoms need sufficient incubation time to diffuse fully. At this time, the experimental steel has been heated to a higher temperature, increasing both the austenite transformation temperature and the end temperature.

According to the results of the thermal expansion experiment, the peak temperatures of ICHAZ, FGHAZ, and CGHAZ are set at 700 °C, 950 °C, and 1300 °C. In addition, the peak temperatures of the transition zone between FGHAZ and CGHAZ are set to 1100 °C and 1200 °C, respectively labeled as TRHAZ I and TRHAZ II.

Plot the SH-CCT curve of the experimental steel using the logarithm of time as the horizontal axis and temperature as the vertical axis, as shown in Figure 4. The SH-CCT curve can reflect the changes in microstructure and properties of experimental steel under the action of welding thermal cycle.^[19] From the

SH-CCT curve, it can be seen that in the cooling rate range of 0.1 °C/s~ 50 °C/s, in the experiment, only martensitic transformation was observed in experimental steel, and the transformation temperature was relatively low. This is due to the high content of Mn element in the experimental steel, which stabilizes undercooled austenite, reducing the martensitic transformation temperature and improving the experimental steel's hardenability. In addition, it can be seen that the microhardness of the experimental steel after undergoing welding thermal cycles is significantly higher than the microhardness of the base material (254 HV). As the cooling rate increases, the microhardness of the experimental steel also increases. When the cooling rate is 0.1 °C/s, the microhardness of the experimental steel is 304 HV; When the cooling rate increases to 50 °C/s, the microhardness of the experimental steel increases to 328 HV. The slight increase in hardness may be due to dislocation density and lath width, which are caused by different cooling rates.

B. The Effect of Different Heat Inputs on the Microstructures and Mechanical Properties of FGHAZ

The welding heat simulation process of FGHAZ is as follows: heat the welding thermal simulation sample at a rate of 100 °C/s to 950 °C, hold it for 1 s, and then cool it to 350 °C with different heat inputs of 10, 15, 20, and 30 kJ/cm. The corresponding $t_{8/5}$ values are 5.5, 12.4, 22, and 49.5 s. The welding thermal cycle curve is shown in Figure 5.

Figure 6 shows the microstructure of FGHAZ under different heat input conditions. It can be seen that the microstructure of FGHAZ is composed of uniform and fine-lath martensite and RA distributed at the prior austenite grain boundary. With the increase of heat input, $t_{8/5}$ increases from 5.5 to 49.5 s, the high-temperature residence time is prolonged during cooling, and the carbon atom diffusion degree is higher, leading to the gradual increase of martensite lath in FGHAZ. The

T_p of FGHAZ welding thermal cycle is slightly higher than A_{c3} . During the heating process, the experimental steel's ferrite lath and tempered martensite are all transformed into austenite, and the austenite grain does not grow significantly. During the cooling process, most of the austenite is transformed into martensite, while the remaining stable austenite is retained at room temperature. Finally, the microstructure of FGHAZ at room temperature is uniformly distributed fine-lath martensite + RA. When subjected to impact load, the fine martensitic lath can increase the number of turning points in the process of crack growth. At the same time, the TRIP effect occurs in RA, which greatly improves the cryogenic impact toughness of FGHAZ.

The -40 °C impact energy and microhardness of FGHAZ under different heat input conditions are shown in Figure 7. It can be seen from Figure 7(a) that even when the temperature of the impact experiment drops to -40 °C, FGHAZ still maintains excellent cryogenic impact toughness. Under heat input conditions of 10, 15, 20, and 30 kJ/cm, the impact energy reaches 247.2, 246.7, 240.5, and 239.5 J. As the heat input increases, the impact energy of FGHAZ tends to decrease, but the decrease is not significant. This result indicates that in the range of 10 to 30 kJ/cm, the change in heat input has a limited impact on the cryogenic impact toughness of FGHAZ.

The hardening effect of FGHAZ is very obvious. When the heat input is 10, 15, 20, and 30 kJ/cm, the corresponding microhardness values are 313.5, 319.2, 309.1, and 298.7 HV, as shown in Figure 7(b). The microhardness values under different heat input conditions are much higher than those of the base material low-temperature medium manganese steel (254 HV). High strength and hardness are prominent characteristics of martensite, which is a solid solution supersaturated with carbon atoms in α -Fe, with the interstitial carbon atoms in the octahedral gap of the α -Fe phase lattice, the square distortion of the lattice is caused and a stress field is formed. This stress field strongly interacts with dislocations, which is one of the important reasons for the increase in strength and hardness of martensite, namely the solid solution strengthening of carbon atoms. In addition, the phase transformation strengthening and aging strengthening of carbon atoms also play a certain role in the strengthening and hardening of martensite.

Figure 8 shows the impact fracture morphology of FGHAZ in the radiation zone at -40 °C under different heat input conditions. It can be found that there are a large number of deep dimples on the impact fracture surface of FGHAZ under four different heat input conditions, and small dimples are evenly distributed around the large dimples. The large and deep dimples created during plastic deformation can effectively absorb a large amount of energy, thereby hindering further crack propagation and improving the cryogenic impact toughness of FGHAZ. Therefore, within the heat input range of 10 to 30 kJ/cm, the fracture mode of FGHAZ is a typical ductile fracture.

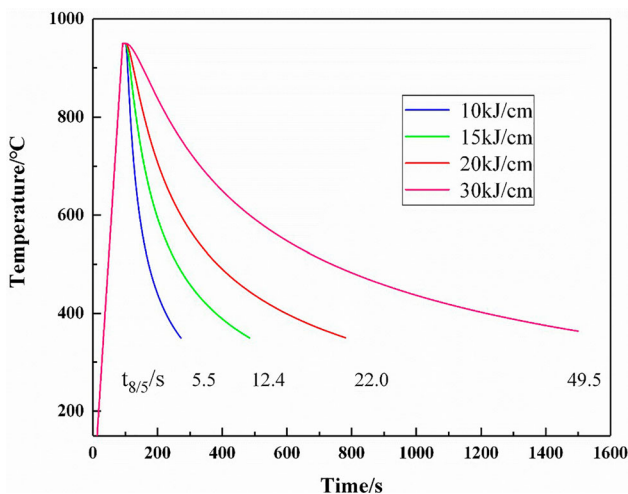


Fig. 5—FGHAZ welding thermal cycle curve of different heat inputs.

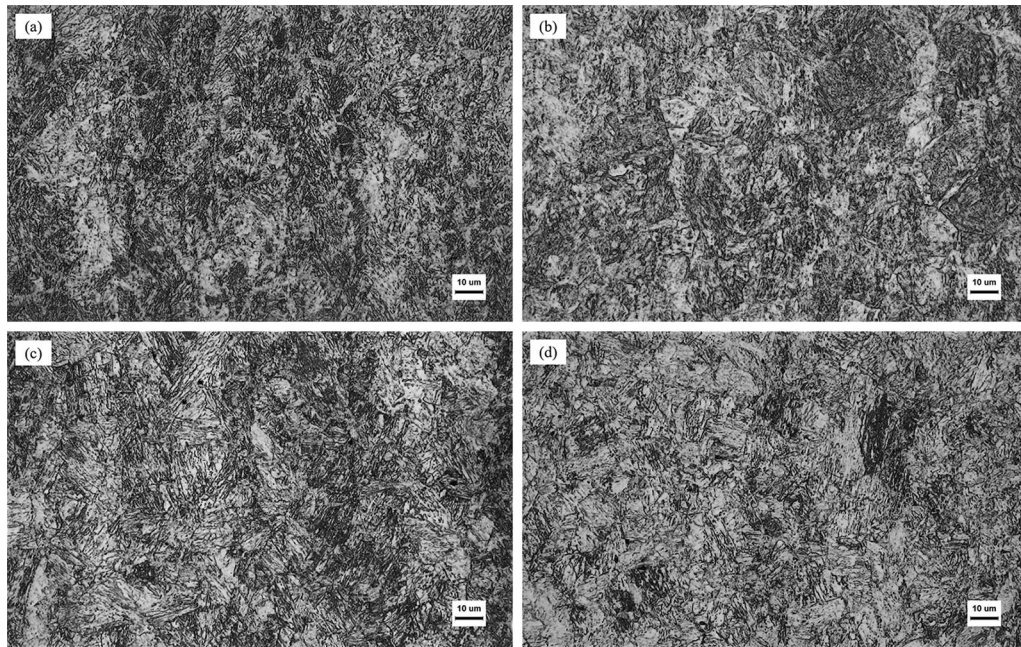


Fig. 6—Microstructure of FGHAZ under different heat inputs. (a) 10 kJ/cm; (b) 15 kJ/cm; (c) 20 kJ/cm; (d) 30 kJ/cm.

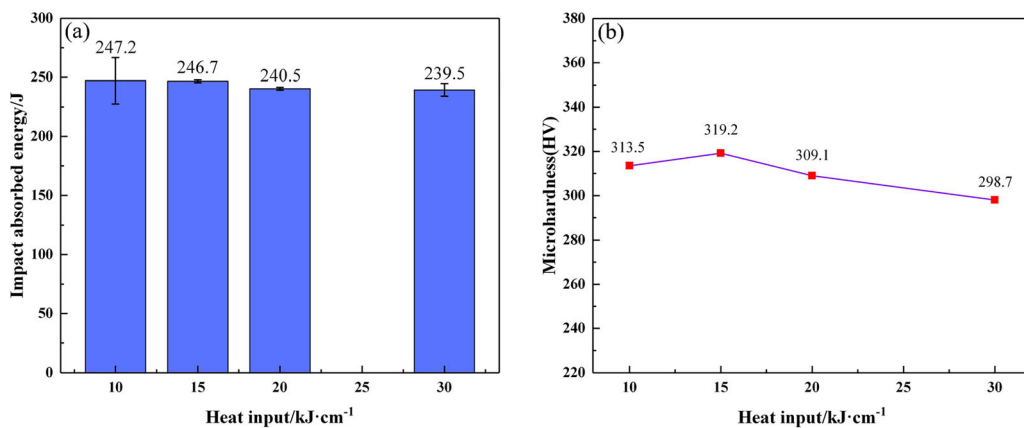


Fig. 7—40 °C impact energy and microhardness of FGHAZ under different heat inputs. (a) – 40 °C impact energy; (b) Microhardness value.

RA has a significant impact on the cryogenic impact toughness of medium-Mn steel, so XRD technology was used to determine the RA content in FGHAZ at room temperature, as shown in Figure 9. Under different heat input conditions, the diffraction patterns of FGHAZ show relatively obvious austenite diffraction peaks, and as the heat input increases, the diffraction peak intensity gradually weakens, as shown in Figure 9(a). Calculate the volume fraction of RA through Eq. [2] as shown in Figure 9(b). The corresponding RA volume fractions for heat inputs of 10, 15, 20, and 30 kJ/cm are 18.47, 16.57, 14.37, and 11.44 pct. It can be seen that the RA volume fraction significantly decreases with the heat input increases.

Although the small heat input corresponds to a higher volume fraction of RA. However, as mentioned earlier, in the range of 10 ~ 30 kJ/cm, the change of heat input has a limited effect on the cryogenic impact toughness of

FGHAZ, so the volume fraction of RA is not the only determining factor for the cryogenic impact toughness of FGHAZ. Many scholars have studied the stability of RA,^[20–23] after undergoing welding thermal cycles and remaining at room temperature, a portion of RA, which was priorly stable at room temperature, transforms into martensite during further cooling. Therefore, it can be reasonably inferred that under low heat input conditions (such as 10 kJ/cm), the stability of RA retained at room temperature for FGHAZ is insufficient to maintain its existence at – 40 °C.

Figure 10 shows the EBSD crystal characteristics of FGHAZ. As shown in Figure 10(a), the prior austenite grain size in FGHAZ is between 4 and 10 μm. Figure 10(b) shows the distribution of FGHAZ grain boundaries, and the proportion of high-angle grain boundaries in FGHAZ is 37.4 pct. Microcracks are severely hampered or even stopped when they encounter

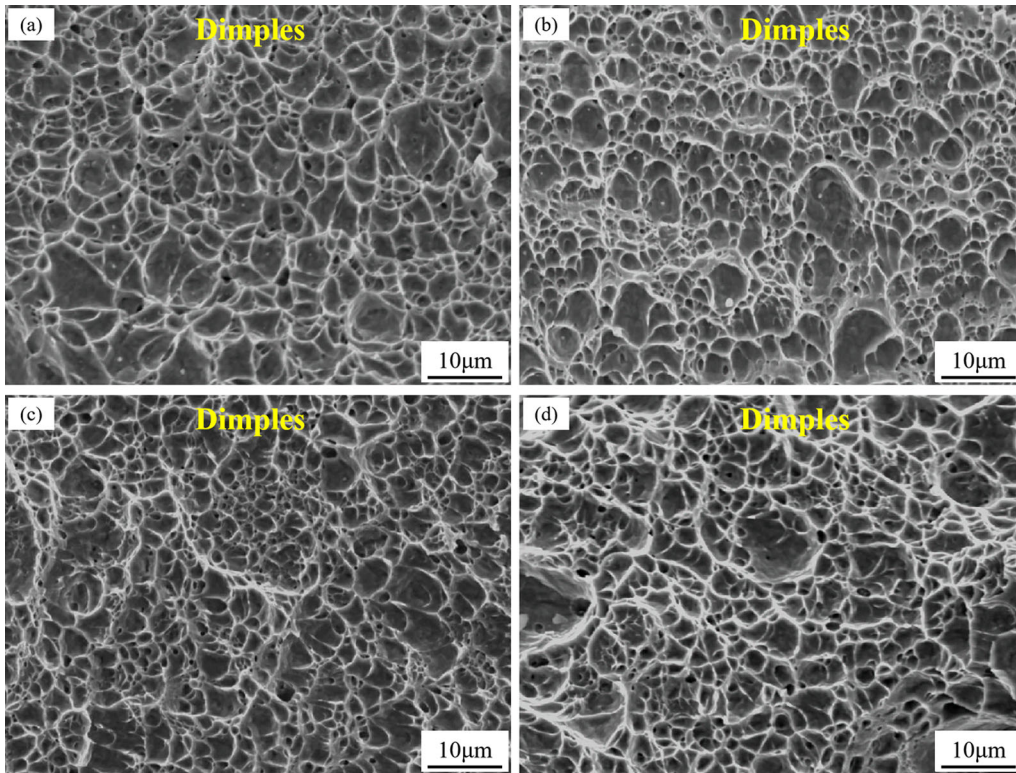


Fig. 8— 40 °C impact fracture morphology of FGHAZ under different heat inputs. (a) 10 kJ/cm; (b) 15 kJ/cm; (c) 20 kJ/cm; (d) 30 kJ/cm.

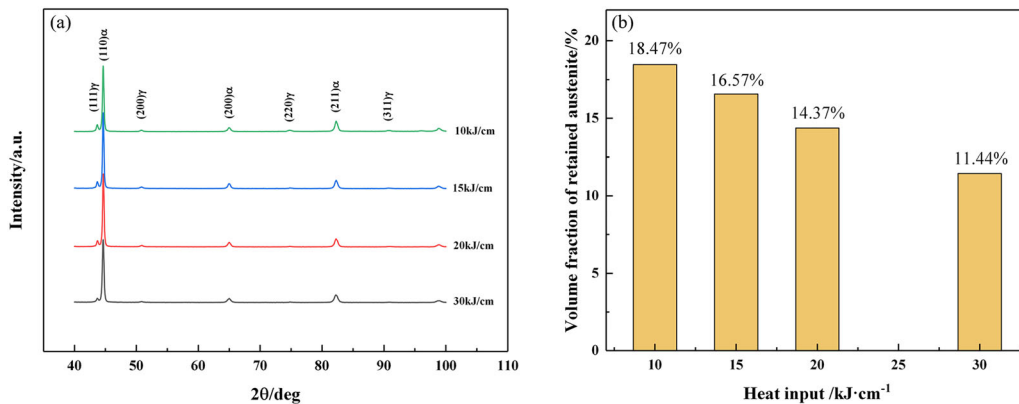


Fig. 9—XRD analysis results of FGHAZ at room temperature. (a) XRD diffraction pattern; (b) RA volume fraction.

high-angle grain boundaries during propagation. At this point, a greater stress concentration is required to allow the microcrack to cross the grain boundary and reach the next grain. In Figure 10(c), gray represents martensite, and red represents RA. It can be seen that RA is distributed in the prior austenite grain boundaries (PAGB) in block form, and some RA is distributed between martensitic lath in lath or film form, parallel to martensitic lath. Martensite or RA with a grain boundary angle difference greater than 15 deg in the microstructure can be defined as two different subgrains.^[24] Figure 10(d) shows the distribution of FGHAZ subgrain size, with an equivalent subgrain size

of 2.6 μm . The fine subgrains and prior austenite grains improve cryogenic impact toughness to some extent.

C. The Effect of Different Heat Inputs on the Microstructures and Mechanical Properties of CGHAZ

The welding heat simulation process of CGHAZ is as follows: heat the welding thermal simulation sample at a rate of 100 °C/s to 1300 °C, hold it for 1 s, and then cool it to 350 °C with different heat inputs of 10, 15, 20, and 30 kJ/cm. The corresponding $t_{8/5}$ values are 5.5, 12.4, 22, and 49.5 s. The welding thermal cycle curve is shown in Figure 11.

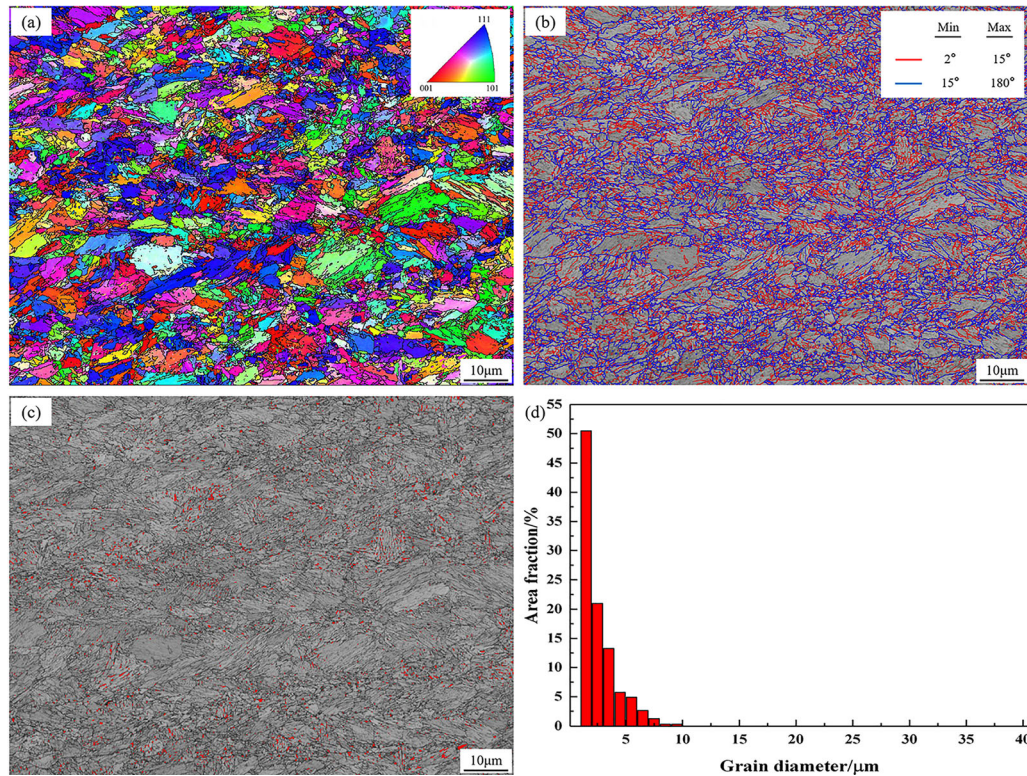


Fig. 10—Crystallographic characteristics of FGHAZ($E = 10 \text{ kJ/cm}$). (a) Orientation map; (b) Grain boundary distribution map; (c) Quality map; (d) Sub grain size distribution map.

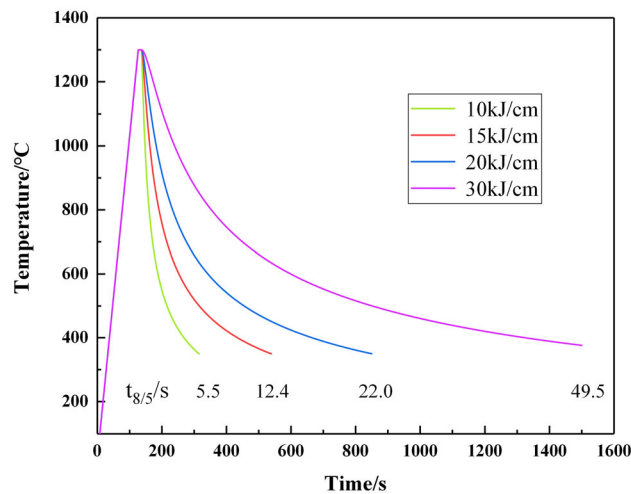


Fig. 11—CGHAZ welding thermal cycle curve of different heat inputs.

Figure 12 shows the microstructure of CGHAZ under different heat input conditions. The microstructure of CGHAZ is coarse lath martensite. With the increase of heat input, the martensite coarsens and the prior austenite grains grow seriously. The T_p of CGHAZ welding thermal cycle is high, even under small heat input conditions (such as 10 kJ/cm , $t_{8/5}$ is only 5.5 s), the incubation time is very short, and carbon atoms can still fully diffuse. The coarse lath martensite structure in CGHAZ means that the area has higher hardness and

lower plasticity and toughness, which leads to embrittlement and microcracks in CGHAZ during service and is a weak part of the mechanical properties of welded joints.

The -40°C impact energy and microhardness of CGHAZ under different heat inputs are shown in Figure 13. As shown in Figure 13(a), the impact energy of CGHAZ decreases with the increase of heat input at -40°C . Coarse lath martensite and prior austenite grains have very limited resistance to crack growth. Under the heat inputs of 10 , 15 , and 20 kJ/cm , the CGHAZ impact energy can only be kept at about 66 J , and the impact energy in this area is far lower than that of the base metal. Especially under the energy condition of 30 kJ/cm welding, the extremely high T_p combined with the long high-temperature residence time results in the impact power of CGHAZ of only 49.7 J , which is even less than a quarter of FGHAZ.

The microhardness of CGHAZ is relatively high and is not significantly affected by heat input, which is consistent with the results of thermal expansion experiments. As shown in Figure 13(b). The microhardness of CGHAZ under all four heat input conditions is above 320 HV , so it is the local hardening zone of the welded joint, just like FGHAZ.

The impact fracture morphology of CGHAZ in the radiation zone at -40°C is shown in Figure 14. There are many cleavage facets on the impact surface, and several dissociation steps combine to form river and fan-shaped patterns. As the heat input increases, the size of the dissociation facet increases, and the river pattern

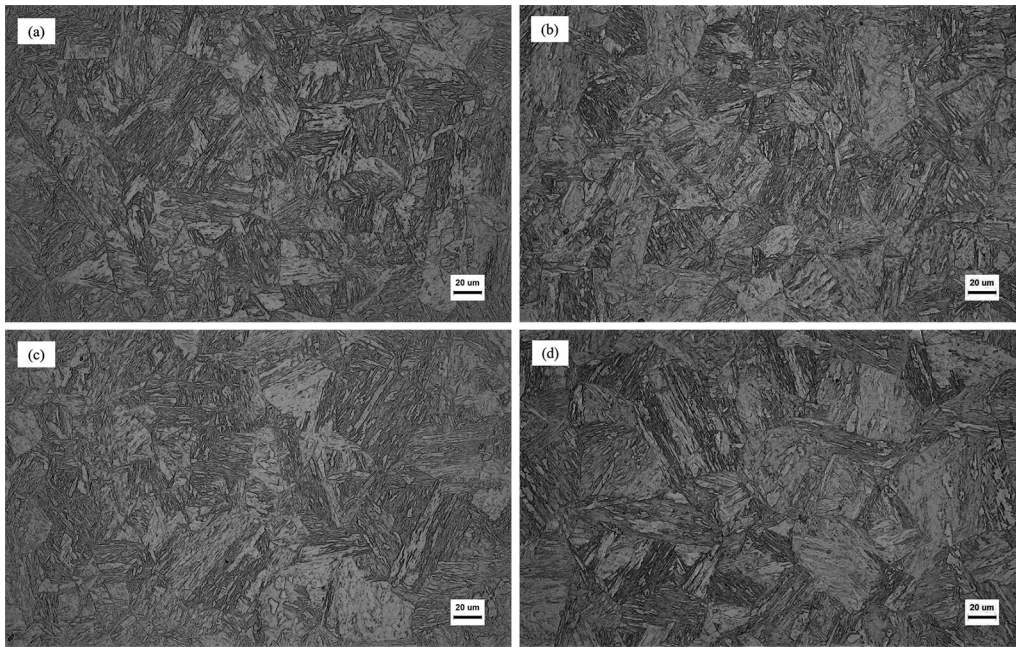


Fig. 12—Microstructure of CGHAZ under different heat inputs. (a) 10 kJ/cm; (b) 15 kJ/cm; (c) 20 kJ/cm; (d) 30 kJ/cm.

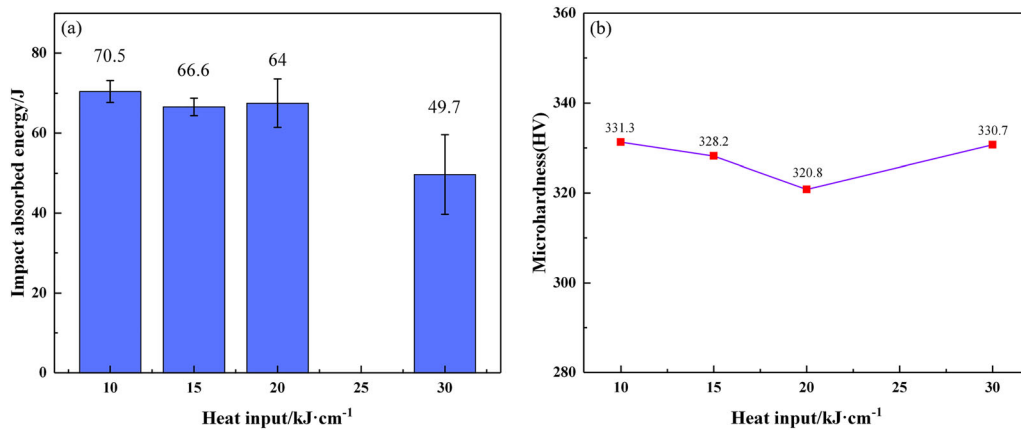


Fig. 13— 40 °C impact energy and microhardness of CGHAZ under different heat inputs. (a) – 40 °C impact energy; (b) Microhardness value.

becomes more apparent. When the heat input is 10, 15, and 20 kJ/cm, dimples of varying sizes are distributed on the impact surface, Figure 14 yellow dashed part. In addition, it can be observed that the higher the heat input, the smaller and fewer dimples, and the fracture mode gradually transitions from quasi-dissociative fracture to cleavage fracture. When the heat input further increases to 30 kJ/cm, the fracture mode of CGHAZ completely transforms into a typical cleavage fracture, with an impact toughness of 49.7 J at – 40 °C.

The EBSD technology was used to study the crystal orientation and grain boundary distribution of CGHAZ under different heat input conditions, as shown in Figure 15. The crystal structure of martensite is body-centered cubic, and microcracks mainly propagate as dissociation planes. When microcracks reach grain boundaries, there is a significant deceleration phenomenon. The deceleration process of microcracks is

related to the orientation of the grains. Therefore, the difference in grain boundary orientation between dissociation planes is the main factor affecting the propagation rate of dissociation cracks.^[25,26]

The high-angle grain boundaries in CGHAZ are mainly PAGB, martensitic packet, and block boundaries; the low-angle grain boundary is mainly the martensite lath boundary parallel to each other in the martensite packet and block.^[27] With the increase of heat input and high-temperature residence time, the prior austenite grain continues to grow, and the martensite lath is merged and widened, forming martensite packets and blocks, resulting in a decrease in the number of high-angle grain boundaries and an increase in the proportion of small angle grain boundaries. The statistical results are shown in Figures 15(c), (f), (i), indicating that the ability of CGHAZ to resist dissociation crack

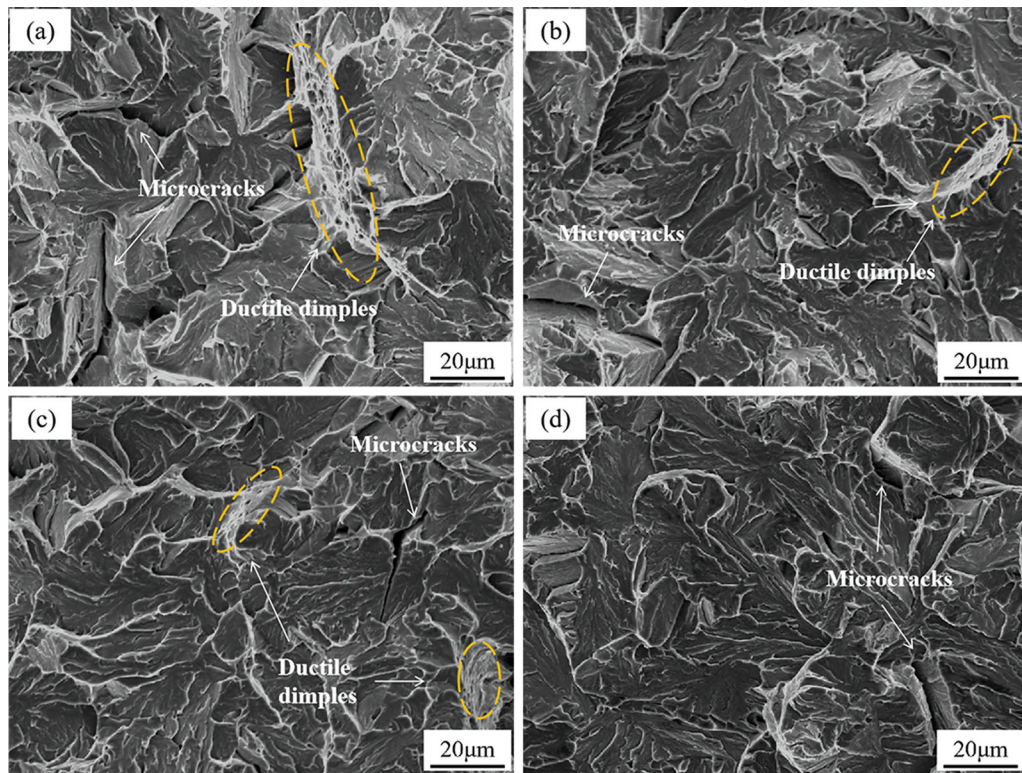


Fig. 14—Impact fracture morphology at $-40\text{ }^{\circ}\text{C}$ of CGHAZ under different heat inputs. (a) 10 kJ/cm; (b) 15 kJ/cm; (c) 20 kJ/cm; (d) 30 kJ/cm.

propagation is weakened, and its cryogenic impact toughness deteriorates.

D. The Effect of Different Peak Temperatures on the Microstructure and Properties of HAZ

Under the condition of $E = 15\text{ kJ/cm}$, the effect of T_p on the microstructure and properties of HAZ was studied. The welding thermal cycle curve is shown in Figure 16. The specific experimental process is as follows: heat the welding thermal simulation samples at a rate of $100\text{ }^{\circ}\text{C/s}$ to $700\text{ }^{\circ}\text{C}$, $950\text{ }^{\circ}\text{C}$, $1100\text{ }^{\circ}\text{C}$, $1200\text{ }^{\circ}\text{C}$, and $1300\text{ }^{\circ}\text{C}$, keep them warm for 1 s, and then cool them to $350\text{ }^{\circ}\text{C}$ at a rate of 15 kJ/cm heat input, corresponding to $t_{8/5}$ of 12.4 s.

The microstructure of the experimental steel simulated welding ICHAZ, FGHAZ, TRHAZ I, TRHAZ II, and CGHAZ is shown in Figure 17. The T_p of ICHAZ is between Ac_1 and Ac_3 , belonging to the incomplete recrystallization zone. The microstructure at room temperature is ferrite + martensite + RA, and the structure is uneven, as shown in Figure 17(a). The T_p of FGHAZ is slightly higher than Ac_3 , which is equivalent to a short normalizing treatment of the experimental steel. The microstructure at room temperature is fine-lath martensite + RA, and the prior austenite grain is uniform and fine, as shown in Figure 17(b). The T_p of TRHAZ I is $150\text{ }^{\circ}\text{C}$ higher than that of FGHAZ, the martensitic lath is further widened, the prior austenite grains grow up in varying degrees, and some stable RA is still kept at room temperature, as shown in Figure 17(c). The T_p of

TRHAZ II is further increased, martensitic lath and prior austenite grains are significantly grown, and almost no RA is retained at room temperature, as shown in Figure 17(d). The T_p of CGHAZ is much higher than that of Ac_3 , the prior austenite grains and martensite lath grow seriously. Finally, it is full martensite at room temperature, as shown in Figure 17(e).

The $-40\text{ }^{\circ}\text{C}$ impact energy and microhardness values of HAZ under different T_p conditions are shown in Figure 18. The impact energies of ICHAZ, FGHAZ, TRHAZ I, TRHAZ II, and CGHAZ at $-40\text{ }^{\circ}\text{C}$ are 226.1, 246.7, 239.6, 145.4, and 66.6 J, respectively, as shown in Figure 18(a). FGHAZ has the best low-temperature impact toughness, followed by TRHAZ I. The impact absorption energy value of TRHAZ II demonstrates the transition effect of impact toughness changes between FGHAZ and CGHAZ. In terms of microhardness, FGHAZ, TRHAZ I, TRHAZ II, and CGHAZ are all localized hardening regions, with microhardness values of 319.2, 339.5, 332.6, and 328.2 HV, TRHAZ I has highest degree of hardening, as shown in Figure 18(b). As the T_p of ICHAZ is slightly higher than Ac_1 , only part of the ferrite undergoes phase transformation during heating, and the microstructure composition after cooling to room temperature is basically the same as that of the base metal. The difference is only that the size of the ferrite lath, the number of martensite, and the volume fraction of RA change. Therefore, the apprior microhardness value of ICHAZ 268.8 HV is not significantly higher than that of the base metal (254 HV).

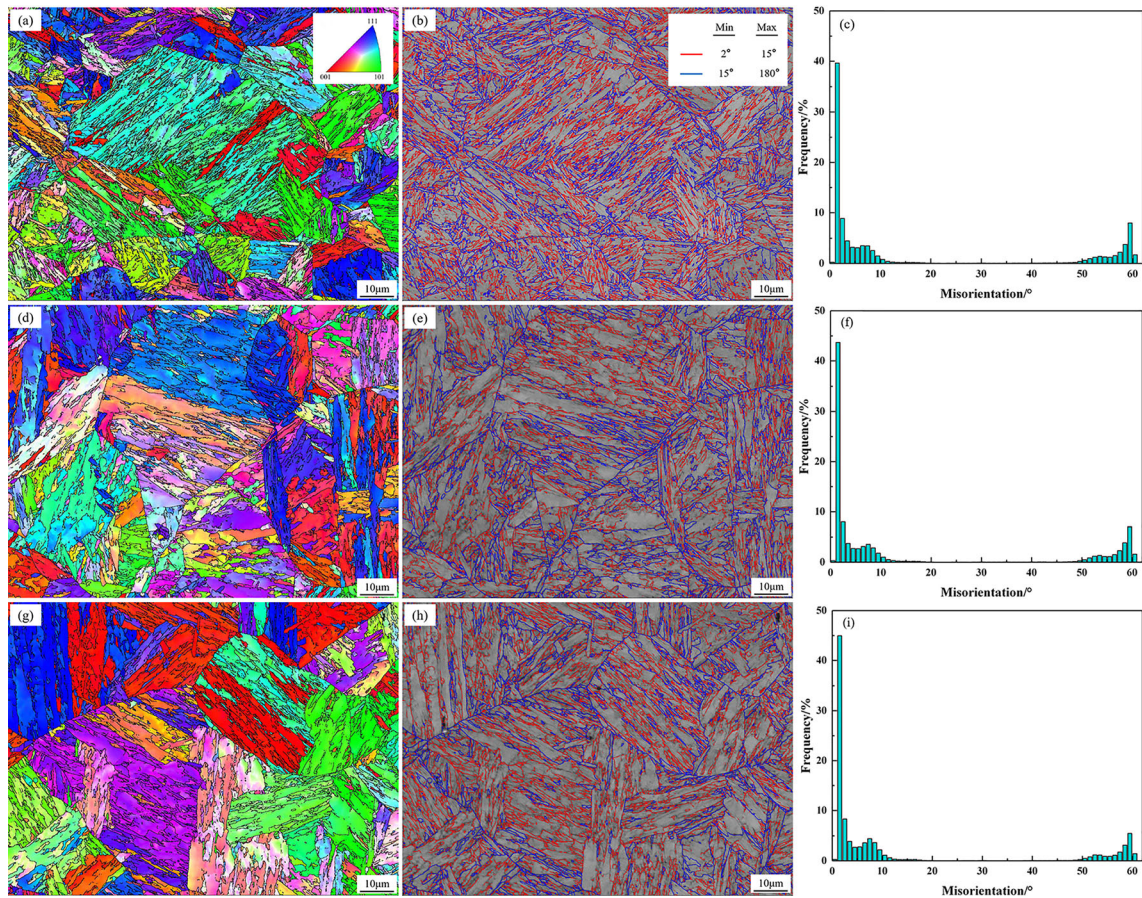


Fig. 15—Crystallographic characteristics of CGHAZ under different heat inputs analyzed by EBSD. (a), (b), (c) 10 kJ/cm; (d), (e), (f) 20 kJ/cm; (g), (h), (i) 30 kJ/cm. (d), (g) orientation map; (b), (e), (h) Grain boundary distribution map; (c), (f), (i) Statistical map of grain boundary orientation difference.

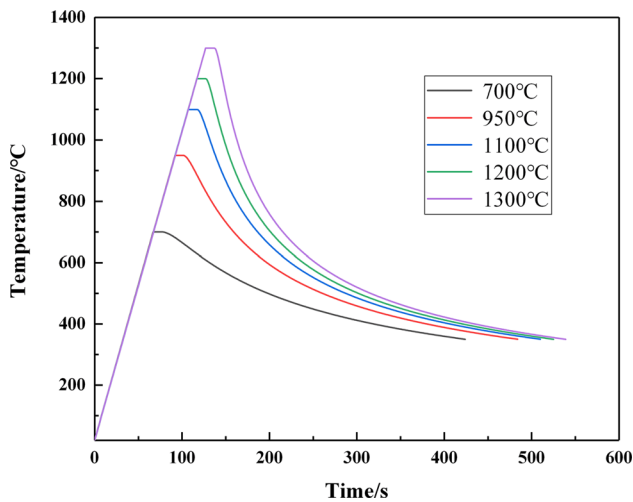


Fig. 16—Welding thermal cycle curve of experimental steel under different T_p conditions ($E = 15$ kJ/cm).

The hardness order of each phase in the HAZ microstructure is: martensite > austenite > ferrite, and the changes in the size and content of each phase result in differences in the microhardness of each HAZ zone. For martensite, its microhardness mainly depends on its

carbon content. The higher the carbon content of martensite, the more obvious the strengthening effect of interstitial carbon atoms, and the higher the microhardness. However, new studies have shown that the microhardness of martensite is also significantly affected by the size of martensite packets and blocks within the prior austenite grains. This can be explained by the fact that the boundaries of martensite packets and blocks are usually large angle grain boundaries, which can strongly hinder dislocation movement, leading to a significant increase in martensite hardness.^[28] Compared with CGHAZ with a microstructure of all martensite, TRHAZ I with a volume fraction of 10.84 pct RA has the most severe hardening. It can be reasonably inferred that the martensite packet and block sizes of TRHAZ I are smaller than those of CGHAZ, resulting in more severe microstructure hardening. Although RA has a softening effect on TRHAZ I, the softening effect produced by a 10.84 pct volume fraction of RA is far from sufficient to offset the hardening effect caused by small martensitic packets and blocks. Therefore, overall, the hardening degree of TRHAZ I microstructure is still more severe than that of CGHAZ.

Figure 19 shows the morphology of the -40 °C impact fracture radiation zone of each HAZ under different T_p conditions. The impact fracture surfaces of

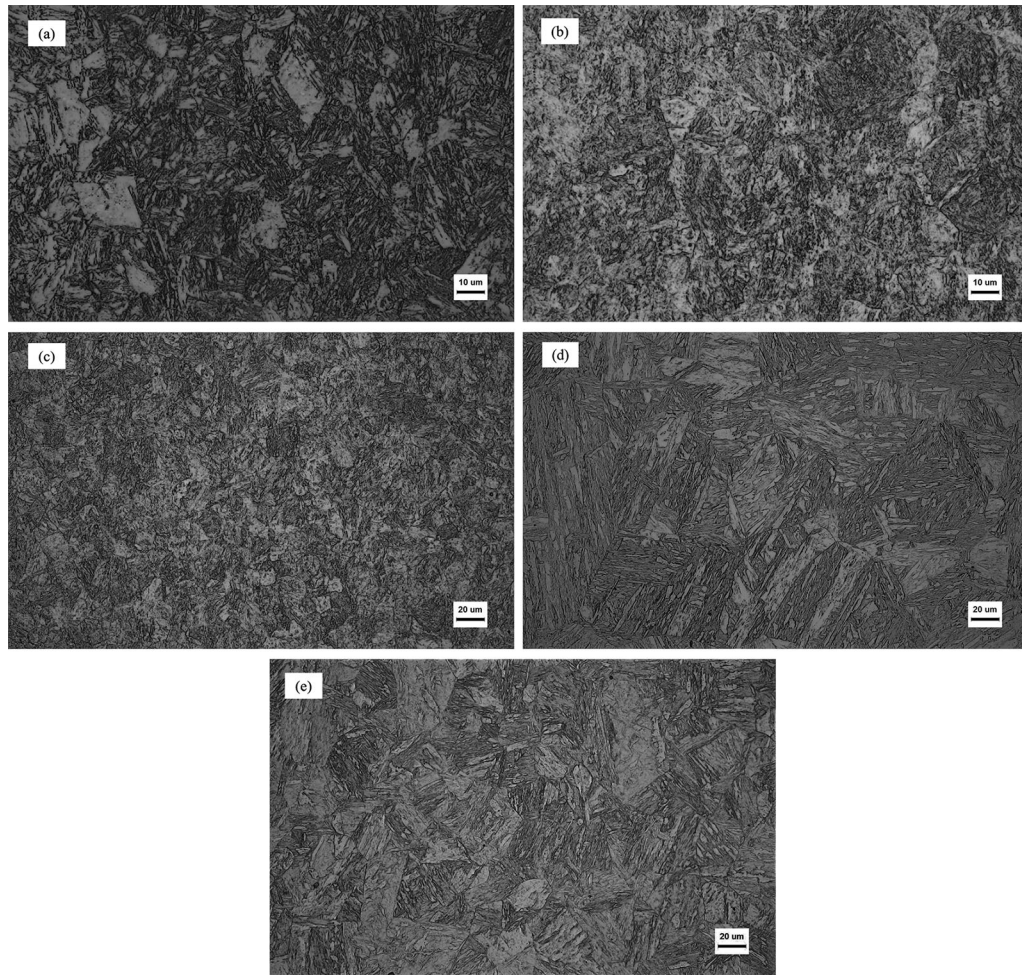


Fig. 17—Metallographic structure of HAZ under different T_p conditions ($E = 15 \text{ kJ/cm}$). (a) ICHAZ; (b) FGHAZ; (c) TRHAZI; (d) TRHAZII; (e) CGHAZ.

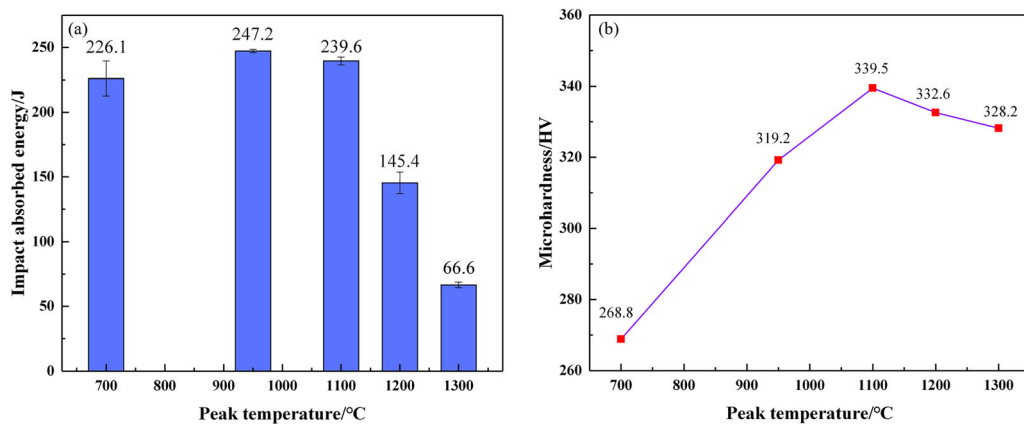


Fig. 18—40 °C impact energy and microhardness of HAZ under different T_p conditions ($E = 15 \text{ kJ/cm}$). (a) – 40 °C impact energy; (b) Microhardness value.

ICHAZ, FGHAZ, and TRHAZ I are distributed with a large number of dimples of varying depths, which are typical ductile fractures, as shown in Figures 19(a) through (c). The impact fracture surface of TRHAZ II exhibits dissociation of small fac, tearing edges, and

small dimples. The river pattern is short and has few tributaries, and its fracture mode is quasi-dissociation fracture between ductile fracture and cleavage fracture, as shown in Figure 19(d). The river pattern on the impact fracture surface of CGHAZ is more obvious

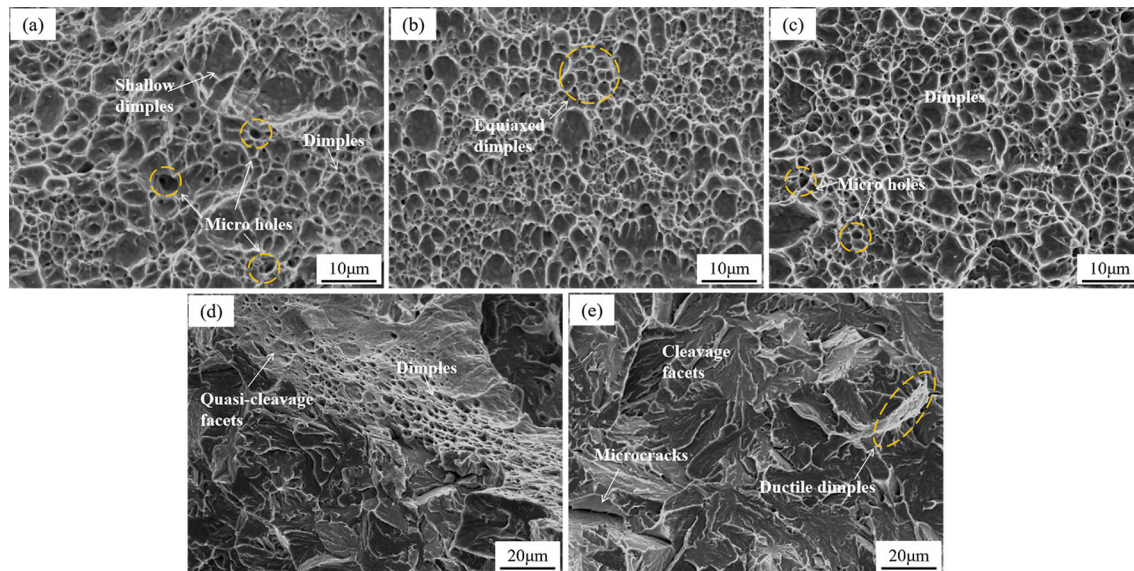


Fig. 19—Impact fracture morphology at $-40\text{ }^{\circ}\text{C}$ of HAZ under different T_p conditions ($E = 15\text{ kJ/cm}$). (a) ICHAZ; (b) FGHAZ; (c) TRHAZI; (d) TRHAZII; (e) CGHAZ.

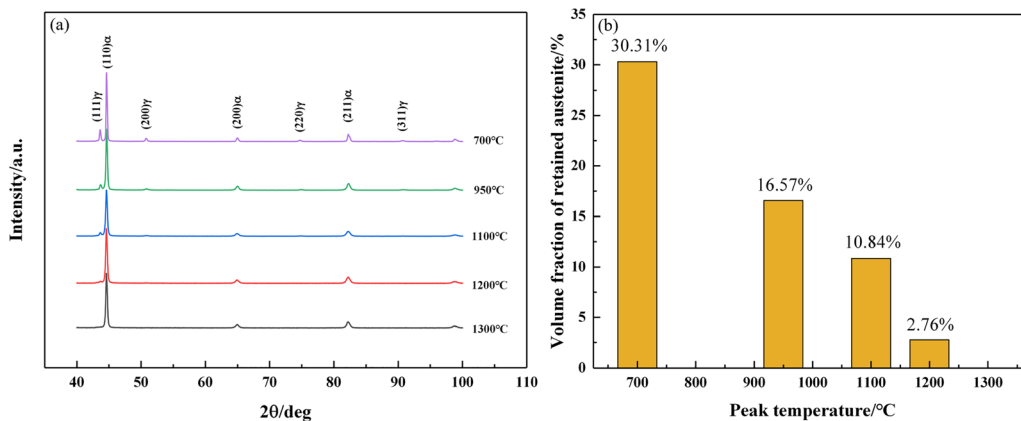


Fig. 20—XRD analysis results of HAZ under different T_p conditions ($E = 15\text{ kJ/cm}$). (a) XRD diffraction pattern; (b) RA volume fraction.

than that of TRHAZ II, and the dissociation facet is further elongated, which is a cleavage fracture, as shown in Figure 19(e).

The XRD diffraction patterns and RA volume fraction of HAZ under different T_p conditions are shown in Figure 20. As T_p increases, the intensity of austenite diffraction peaks gradually decreases. When T_p increases to $1200\text{ }^{\circ}\text{C}$ and $1300\text{ }^{\circ}\text{C}$, the characteristic peaks of austenite almost do not exist, as shown in Figure 20(a). After calculation, the RA volume fractions of ICHAZ, FGHAZ, TRHAZ I, and TRHAZ II were 30.31, 16.57, 10.84, and 2.76 pct, respectively, while CGHAZ did not have RA, as shown in Figure 20(b).

The fine structure of HAZ was characterized using TEM, as shown in Figure 21. The T_p of ICHAZ is between A_{c1} and A_{c3} , during welding heating, the tempered martensite of the experimental steel is unchanged, the ferrite is partially dissolved in austenite, and the remaining ferrite lath continues to grow. The

newly generated austenite is rich in C. Still, not Mn, and transforms into martensite during cooling, so the ICHAZ microstructure is composed of coarse α -ferrite, RA (strip, block, and granular), and martensite (tempered martensite + newly generated martensite). The microstructure of ICHAZ is very uneven, as shown in Figure 21(a). The microstructure of FGHAZ consists of fine-lath martensite with high dislocation density + submicron film-like RA. RA film exists between and parallel to martensite lath, as shown in Figure 21(b). The bright field image, dark field image, and SAED spectrum of RA are shown in Figures 21(d) through (f). The width of RA film is between 40 and 90 nm. The small lath martensite and film-like RA greatly improve the cryogenic impact toughness of FGHAZ. The T_p of CGHAZ reaches $1300\text{ }^{\circ}\text{C}$, and the prior austenite grains grow seriously, as shown in Figure 21(c). The lath martensite with high dislocation density forms multiple packet or block structures inside the austenite grains.

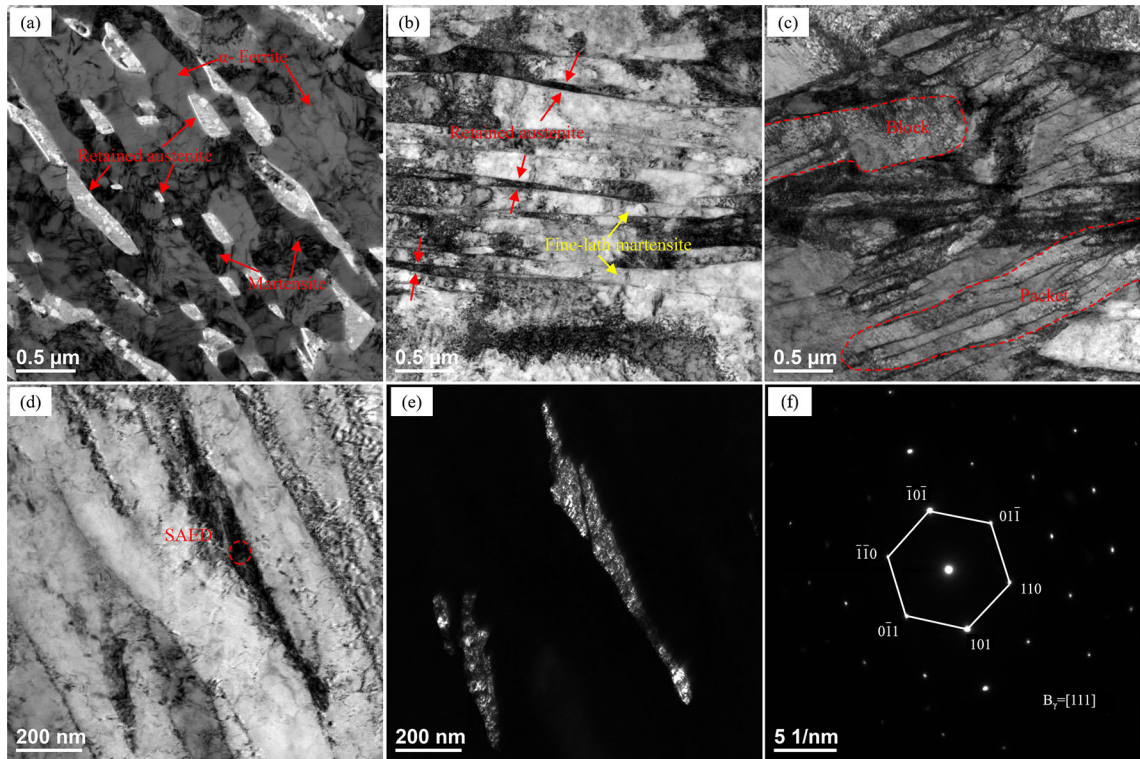


Fig. 21—TEM microstructure of HAZ under different T_p conditions ($E = 15 \text{ kJ/cm}$). (a) ICHAZ; (b) FGHAZ; (c) CGHAZ; (d), (e) RA bright and dark field images in FGHAZ; (f) SAED spectrum of RA.

The coarse lath martensite and the prior austenite grains greatly deteriorate the cryogenic impact toughness of CGHAZ.

As mentioned earlier, the TRIP effect that occurs when RA is subjected to impact loads significantly improves the cryogenic impact toughness of medium-Mn steel. At a heat input of 15 kJ/cm , the volume fraction of RA in the microstructure of ICHAZ is about twice that of FGHAZ, reaching 30.31 pct. However, the impact energy at -40°C is slightly lower than that of FGHAZ. As can be seen from Figure 21(a), RA in ICHAZ mainly exists in the form of lath and block, RA lath width is about $150 \sim 300 \text{ nm}$, while RA in FGHAZ exists in film with a thickness of about 90 nm . $10 \sim 100 \text{ nm}$ is the optimal grain size for RA, and within this range, the stability of RA is moderate. When the RA size is less than 10 nm , its stability is too high, which is not conducive to the occurrence of the TRIP effect. When the size of RA is greater than 100 nm , it is prone to martensitic transformation during the cooling process due to insufficient stability.^[29,30] Therefore, although the volume fraction of RA in ICHAZ is high, during the cooling process to -40°C , a considerable portion of unstable RA transforms into martensite, coupled with the uneven microstructure of ICHAZ, ultimately resulting in a slightly lower cryogenic impact toughness than FGHAZ at -40°C .

IV. CONCLUSIONS

This study used the thermal expansion method to study the phase transformation behavior of medium-Mn low-temperature steel CGHAZ during continuous cooling and plotted the SH-CCT curve. At the same time, a thermal simulation testing machine was used to study the effects of different heat inputs and T_p on the microstructure, microhardness, and cryogenic impact toughness of experimental steel HAZ. The main conclusions are as follows:

- (1) Under the conditions of welding thermal cycling, the starting and ending temperatures of austenitization of the experimental steel are 655°C and 871°C , respectively, which are higher than those in the equilibrium state. In the cooling rate range of $0.1 \sim 50^\circ\text{C/s}$, only martensitic transformation exists.
- (2) In the range of $10 \sim 30 \text{ kJ/cm}$, the heat input has little effect on the cryogenic impact toughness of FGHAZ, and the impact energy at -40°C is around 245 J . Fine-lath martensite slows down the growth rate of microcrack, and stable thin-film RA produces TRIP effect to alleviate local stress concentration, which is the main reason for FGHAZ excellent cryogenic impact toughness.
- (3) Within the heat input range of $10 \sim 30 \text{ kJ/cm}$, as the heat input increases, the fracture mode of CGHAZ gradually transitions from quasi-dissociative fracture to cleavage fracture. Coarse

martensitic lath and prior austenite grains seriously deteriorate the cryogenic impact toughness of CGHAZ. When the heat input is 10 kJ/cm, the CGHAZ impact work at $-40\text{ }^{\circ}\text{C}$ is 70.5 J.

- (4) The microstructure of ICHAZ is very uneven, coupled with the low stability of RA, making its cryogenic impact toughness lower than FGHAZ. TRHAZ I still maintains good cryogenic impact toughness. TRHAZ II fracture mode is a typical quasi-dissociative fracture, which nicely demonstrates the transition effect of cryogenic impact toughness changes between FGHAZ and CGHAZ.

CONFLICT OF INTEREST

On behalf of all authors, the corresponding author states that there is no conflict of interest.

REFERENCES

1. S.H. Chen, M.J. Zhao, X.Y. Li, and L.J. Rong: *J. Mater. Sci. Technol.*, 2012, vol. 28, pp. 558–61.
2. Y.Z. Liu, C.F. Yang, F. Chai, T. Pan, and H. Su: *J. Iron. Steel Res. Int.*, 2014, vol. 21, pp. 956–63.
3. P.P.N. Maia, É.M. Miná, G. Dalpiaz, R.R. Marinho, M.T.P. Paes, M.F. Motta, H.C. Miranda, and C.C. Silva: *J. Market. Res.*, 2023, vol. 24, pp. 1716–32.
4. D.Y. Wu, X.L. Han, H.T. Tian, B. Liao, and F.R. Xiao: *Metall. Mater. Trans. A*, 2015, vol. 46A, pp. 8842–80.
5. S.L. Li, Y.L. Wang, and X.T. Wang: *Mater. Sci. Eng. A*, 2015, vol. 639, pp. 640–46.
6. Z.H. Liao, Y. Dong, Y. Du, X.N. Wang, M. Qi, H.Y. Wu, X.H. Gao, and L.X. Du: *J. Market. Res.*, 2023, vol. 23, pp. 1471–86.
7. J. Chen, M.Y. Lv, Z.Y. Liu, and G.D. Wang: *Mater. Sci. Eng. A*, 2015, vol. 648, pp. 51–56.
8. Y. Zou, Y.B. Xu, Z.P. Hu, X.L. Gu, F. Peng, X.D. Tan, S.Q. Chen, D.T. Han, R.D.K. Misra, and G.D. Wang: *Mater. Sci. Eng. A*, 2016, vol. 675, pp. 153–63.
9. J. Chen, W.N. Zhang, Z.Y. Liu, and G.D. Wang: *Metall. Mater. Trans. A*, 2017, vol. 48A, pp. 5849–59.
10. C.W. Li, Y. Wang, and Y.H. Chen: *J. Mater. Sci.*, 2011, vol. 46, pp. 6424–31.
11. C. Li, Y. Wang, T. Han, B. Han, and L. Li: *J. Mater. Sci.*, 2011, vol. 46, pp. 727–33.
12. X.Y. Qi, L.X. Du, J. Hu, and R.D.K. Misra: *Steel Res. Int.*, 2018, vol. 89, p. 1700422.
13. T. Lahtinen, P. Vilaça, P. Peura, and S. Mehtonen: *Appl. Sci.*, 2019, vol. 9, p. 1031.
14. D. Chinakhov, E. Chinakhova, and A. Sapozhkov: *IOP Conf. Ser.*, 2016, vol. 142, p. 012026.
15. Y.X. Chen, H.H. Wang, H. Cai, J.H. Li, and Y.Q. Chen: *Materials*, 2018, vol. 11, p. 2127.
16. J. Hu, X.Y. Li, Q.W. Meng, L.Y. Wang, Y.Z. Li, and W. Xu: *Mater. Sci. Eng. A*, 2022, vol. 855, p. 143904.
17. Y.Y. Feng, Z.A. Luo, D.H. Zhang, J. Wei, and L.J. Wang: *J. Iron Steel Res.*, 2008, vol. 20, pp. 49–52.
18. Y.Q. Wang, R.H. Duan, J. Hu, Z.A. Luo, Z.Y. Ma, and G.M. Xie: *J. Mater. Process. Technol.*, 2022, vol. 306, p. 117621.
19. X.M. Wang, A.M. Zhao, S.P. Liu, and Z.Y. Bao: *Int. J. Microstruct. Mater. Prop.*, 2021, vol. 15, p. 356.
20. H.S. Yang and H.K.D.H. Bhadeshia: *Scripta Mater.*, 2009, vol. 60, pp. 493–95.
21. Y. Matsuoka, T. Iwasaki, N. Nakada, T. Tsuchiyama, and S. Takaki: *ISIJ Int.*, 2013, vol. 53, pp. 1224–30.
22. Y.B. Xu, Y. Zou, Z.P. Hu, D.T. Han, S.Q. Chen, and R.D.K. Misra: *Mater. Sci. Eng. A*, 2017, vol. 698, pp. 126–35.
23. J. Hu, L.X. Du, W. Xu, J.H. Zhai, Y. Dong, Y.J. Liu, and R.D.K. Misra: *Mater. Charact.*, 2018, vol. 136, pp. 20–28.
24. J. Yoo, K. Han, Y. Park, and C. Lee: *Mater. Chem. Phys.*, 2014, vol. 146, pp. 175–82.
25. A.F. Gourgues: *Mater. Sci. Technol.*, 2002, vol. 18, pp. 119–33.
26. H.J. Yi, D. Li, Y.L. Su, and L.Y. Xu: *Weld. Technique*, 2022, vol. 51, pp. 57–62.
27. Y.L. Zhou, T. Jia, X.J. Zhang, Z.Y. Liu, and R.D.K. Misra: *J. Mater. Process. Technol.*, 2015, vol. 219, pp. 314–20.
28. S. Morito, H. Yoshida, T. Maki, and X. Huang: *Mater. Sci. Eng. A*, 2006, vol. 438–440, pp. 237–40.
29. J.J. Wang and S. Van Der Zwaag: *Metall. Mater. Trans. A*, 2001, vol. 32A, pp. 1527–39.
30. X.D. Tan, Y.B. Xu, X.L. Yang, Z.Q. Liu, and D. Wu: *Mater. Sci. Eng. A*, 2014, vol. 594, pp. 149–60.

Publisher's Note Springer Nature remains neutral with regard to jurisdictional claims in published maps and institutional affiliations.

Springer Nature or its licensor (e.g. a society or other partner) holds exclusive rights to this article under a publishing agreement with the author(s) or other rightsholder(s); author self-archiving of the accepted manuscript version of this article is solely governed by the terms of such publishing agreement and applicable law.